Jong-Hwan Park[1], Sun-Woo Kim[2], So Young Lee[2], Yuri Jung[3], Jae-Chul Ro[3], Seong-Ju Park[2], Hyoung-Juhn Kim[2], Dong Han Seo[2], and Su-Jeong Suh[3]

[1]Sungkyunkwan University College of Engineering
[2]Korea Institute of Energy Technology
[3]Sungkyunkwan University - Suwon Campus

August 31, 2024

Abstract

Metal dichalcogenide based 2D materials, gained considerable attention recently as a hydrogen evolution reaction (HER) electrocatalyst. In this work, we synthesized MoSe2 based electrocatalyst via hydrothermal route with varying phase contents (1T/2H) and respective HER performances were evaluated under the acidic media (0.5M H2SO4), where best HER performance was obtained from the sample consisting of mixed 1T/2H phases, which was directly grown on a carbon paper (167mV at 10mA/cm2) Furthermore, HER performance of electrocatalyst was further improved by in-situ electrodeposition of Pt nanoparticles (0.15 wt%) on the MoSe2 surface, which lead to significant enhancement in the HER performances (133mV at 10mA/cm2). Finally, we conducted DFT calculations to reveal the origin of such enhanced performances when the mixed 1T/2H phases were present, where phase boundary region (1T/2H heterojunction) act as a low energy pathway for H2 adsorption and desorption via electron accumulation effect. Moreover, presence of the Pt nanoparticles tunes the electronic states of the MoSe2 based catalyst, resulting in the enhanced HER activity at heterointerface of 1T/2H MoSe2 while facilitating the hydrogen adsorption and desorption process providing a low energy pathway for HER. These results provide new insight on atomic level understanding of the MoSe2 based catalyst for HER application.

1. Introduction

Green hydrogen has emerged as an important clean energy source for replacing the conventional energy source, such as fossil fuel which could contribute in decreasing the greenhouse effect. Electrochemical water electrolysis (EWE), the process used to generate green hydrogen, consisting of hydrogen evolution reaction (HER) and oxygen evolution reaction (OER), has been widely studied over the decades due to its advantageous merits including high hydrogen production rate and ability to generate high purity hydrogen without other byproducts.[1] However, large amount of energy is needed to split the water, although the theoretical potential for the water electrolysis is 1.23 V, additional energy is required due to the presence of overpotential arising from the electrocatalyst in each HER & OER processes which hinder energy efficient production of hydrogen. Therefore, developing advanced electrocatalyst with lower overpotential with high activity, low charge transfer resistance and excellent electrical conductivity is highly desired for energy efficient, high performing water electrolysis. [2]

Specifically, in HER process, the use of noble catalyst such as Pt/C is widely used as an electrocatalyst, owing to its low overpotential with high activity along with its great conductivity. Yet, the use of expensive, noble metal catalyst is one of the roadblocks in cost effective production of green hydrogen. [3]Therefore, many researches have been directed towards finding a new non-noble metal based electrocatalyst [4] with comparable HER activity of Pt/C catalyst. [5]Recently, various 2D Materials have been widely studied as a promising candidate for HER. Amongst the 2D materials, MoSe2 metal dichalcogenides based 2D material gained considerable interests as a promising candidate for HER due to its tunable d-spacing with lamellar structure facilitating the ion transport and tunable conductivity provided by controlling the phase of the

MoSe$_2$(metallic-semiconducting transition). [6] Amongst the phases in metal dichalcogenide based 2D materials, 2H phase (semiconducting phase) shows low HER performance compared to the 1T phase (metallic phase) due to its lower conductivity.[6-b] Therefore, careful optimization of the phase and structure of the MoSe$_2$ is essential for high HER performances. Moreover, MoSe$_2$ with the optimized 1T and 2H mixed phases, have shown to improve the HER activity,[6-a] Although further study is needed to investigate the origin of the high HER performance induced by mixed phase of metal dichalcogenide based electrocatalyst such as MoSe$_2$. [6] Previous studies have explored various strategies to enhance the catalytic performance of MoSe$_2$ for the HER. For example, Jiang et al.[7] demonstrated the synthesis of 1T-MoSe$_2$ nanosheets with expanded interlayer spacing, which showed superior electrochemical performance compared to conventional MoSe$_2$. They reported a low overpotential of 179 mV and a small Tafel slope of 78 mV/dec, attributing these improvements to the high conductivity and increased number of active sites in the 1T phase. Qu et al. [8] introduced MoSe$_2$/Mo core-shell 3D hierarchical nanostructures, which significantly improved HER efficiency. Their study highlighted that the 1T-MoSe$_2$/Mo core-shell structures exhibited a low Tafel slope of 34.7 mV/dec, suggesting enhanced electron transfer efficiency between the catalyst and electrode. Li et al.[9] investigated the effects of S-doping on MoSe$_2$, showing that doping induces a phase transformation to 1T-MoSe$_2$. This transformation has led to a high purity of the 1T phase, resulting in a low overpotential of 167 mV and a Tafel slope of 54 mV/dec, thereby enhancing HER performance. Additionally, Ren et al. [10]developed V-doped MoSe$_2$ nanosheets confined on carbon black (V-MoSe$_2$/CB) using a sol–gel process. This approach prevented agglomeration and yielded ultra-thin nanosheets with short vertical lattice arrays. The V-MoSe$_2$/CB catalyst exhibited improved HER activity with a small overpotential of 166 mV at 10 mA/cm^2 and a Tafel slope of 65 mV/dec, attributed to optimized electronic structure and enhanced electrocatalytic performance. These studies have collectively illustrated various methods to maximize the catalytic efficiency of MoSe$_2$-based materials for HER. Furthermore, often metal-based dopants could be introduced to improve the HER performances of the metal dichalcogenide based electrocatalyst, where Pt nanoparticles/dopant has shown to be effective in enhancing the HER performances. [11]

Besides the development of the high performing electrocatalyst, HER performances can be affected by the method in which electrocatalyst deposition takes place on the current collector. Conventionally, electrocatalyst deposition is often carried out via drop-casting process, where electrocatalyst is often mixed with non-conductive binders such as Nafion or PVDF, which are then pasted onto a conductive current collector. The used of non-conductive binders often, obstructs the active sites of the electrocatalyst while increasing the resistance in the electrodes. In contrast, direct growth of electrocatalyst on the current collector is often favored due to its fast electron transfer between the electrocatalyst and the substrate, resulting in enhanced HER activity with long-term stability without the masking effect which could be more favorable method of electrocatalyst deposition compared to the conventional process. [12]

Finally, media in which HER takes place, is an important factor determining the HER performances. Generally, use of the pure water induces high overpotential of water electrolysis due to its high electrolyte resistance. Often, H$_2$SO$_4$ or KOH based electrolytes are used, which reduce electrolyte resistance, to increase the efficiency of water electrolysis and to decrease the overpotential. Especially, water electrolysis under acidic operation conditions has advantages such as high current density (~2 A/cm^2) and low gas crossover compared to alkaline water electrolysis (AWE). Therefore, water electrolysis under acidic media is favorable for the designing of compact water electrolysis cell.[13]

Using the merits of above-mentioned materials/techniques, in this study, we synthesized mixed phase 1T/2H MoSe$_2$ powder via hydrothermal process where phase contents in MoSe$_2$ were controlled by the synthesis time, then the HER performances of the resultant electrocatalysts were first evaluated. The best HER performances were demonstrated by the samples with synthesis time of 36 h which exhibited overpotential of 177 mV at 10 mA/cm^{2}under the acidic media (0.5 M H$_2$SO$_4$) which was chosen as optimum synthesis time. Then, we synthesized 1T/2H mixed phases of MoSe$_2$ directly grown on a 3D porous carbon paper via hydrothermal synthesis process for 36h, where enhanced HER performances of 167 mV at 10 mA/cm^2 were observed compared to the conventional deposition process using a binder. Moreover, we conducted an in-situ electrodeposition of Pt nanoparticle on MoSe$_2$, using the chronopotentiometry technique which

resulted in excellent HER performances with low overpotential of 133 mV at 10 mA/cm^2, compared to the Pt-free, pristine MoSe$_2$ powder. Finally, we conducted a thorough theoretical study (DFT calculation) on varying HER performances under various 1T/2H phase conditions to explore the origin of phase dependent HER performance in MoSe$_2$ based electro catalyst as well as under the presence of Pt decoration on the mixed phases of MoSe$_2$, shedding a light on atomistic insight on HER performances of 2D material based electrocatalyst such as MoSe$_2$.

not-yet-known not-yet-known

not-yet-known

unknown

2. Results and Discussion

2.1 In-situ Pt decorated, (1T/2H) MoSe₂synthesis on a carbon paper
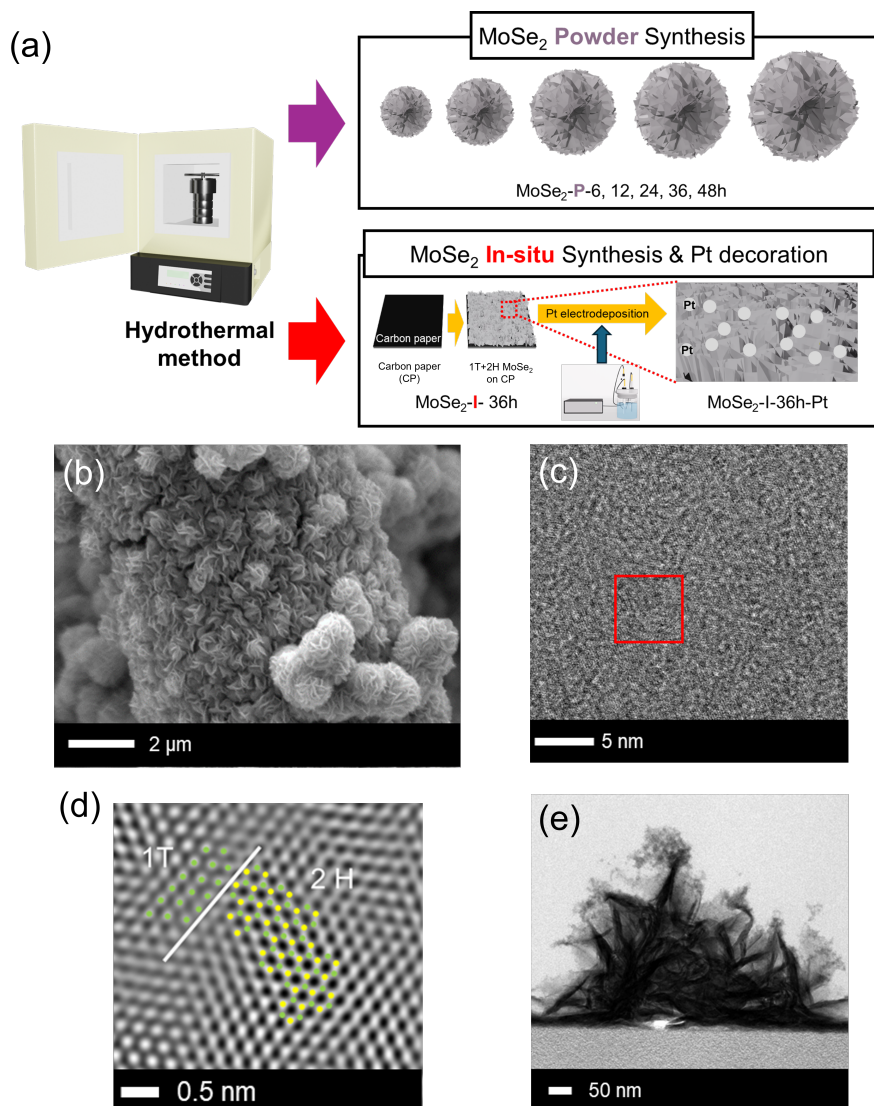
Figure 1. a) Schematic of the synthesis of MoSe$_2$ bulk powder and MoSe$_2$ directly grown on a carbon paper.

b) Secondary electron microscope (SEM) image of $MoSe_2$-I-36h. c) High-resolution transmission electron microscope (HR-TEM) image. d) Masked fast Fourier transform (FFT) of the marked red box in c); green atom: Mo, yellow atom: Se, e) Cross-section image of TEM of $MoSe_2$-I-36h-Pt. $MoSe_2$-I-36h before and after Pt decoration.

Figure 1 (a) presents the schematic of $MoSe_2$powder synthesis and in-situ grown $MoSe_2$ on a carbon paper. In brief, to produce the powder-type $MoSe_2$, a solution containing 1.645 g $Na_2MoO_4[?]2H_2O$, 1.5492 g Se powder, and 0.2595 g $NaBH_4$ dissolved for 0.5 h in a mixture of 25 mL deionized water and 25 mL ethanol was prepared. Subsequently, the dark-colored solution was transferred to a 100 mL stainless steel autoclave and heated to 200°C, maintained at varying synthesis time. To obtain in-situ grown $MoSe_2$ on a carbon paper, the carbon paper was added to the mixed solution. Pt nanoparticles were decorated on the $MoSe_2$ surface using chronopotentiometry at 10 mA cm^{-2} for 100 h. It was confirmed using ICP-MS that the amount of Pt loading was about 0.15 wt%. (**Table S1**) Powder $MoSe_2$ and in-situ grown $MoSe_2$ were denoted as $MoSe_2$-P-X and $MoSe_2$-I-X, respectively, where X represents the synthesis time.

Through SEM analysis, we observed variations in morphologies of $MoSe_2$ powder dependent on the synthesis time. For $MoSe_2$-P-1 h, irregular particles shapes/sizes with undesired composition of $MoSe_{2.86}$ were observed, as shown in **Figure S1** (a) and **Figure S2** (a). The compositions of $MoSe_2$-P-6h, $MoSe_2$-P-12h, $MoSe_2$-P-24h, $MoSe_2$-P-36h, and $MoSe_2$-P-48h were analyzed by SEM-EDS shown in**Fig. S2** (b)–(f). The obtained compositions were $MoSe_{2.05}$, $MoSe_{1.97}$, $MoSe_{2.02}$, $MoSe_{1.96}$, $MoSe_{2.00}$, respectively. $MoSe_2$ nanosheets in **Fig. S1** (b)–(f) were generated with increasing synthesis time to 6 h. The flower-like $MoSe_2$ nanosheet was obtained from 12 h onwards. **Figure S3** shows XRD spectra of $MoSe_2$ powder samples. For $MoSe_2$-P-2H, peaks at 13.1deg, 31.4deg, 37.8deg, and 55.94deg matched to (002), (100), (103), and (110) planes of $MoSe_2$-2H (JCPDS 00-029-0914). In the case of MoSe-P-1 h, the peaks were corresponded to Se (JCPDS 01-086-2246) revealing the incomplete synthesis of $MoSe_2$. When the synthesis time was more than 6 h, we observed the absence of the Se peak as well as the peak corresponding to (103) plane of $MoSe_2$ originating from the 2H phase. Moreover, the shift and broadening of peaks corresponding to (002) and (100) planes of $MoSe_2$ were observed, indicating the presence of mixed 1T and 2H phases of $MoSe_2$.[6-a] **Figure S4** exhibits Raman analysis of the $MoSe_2$-P samples. Intensity of a peak at 239 cm^{-1}, corresponding to A_{1g} of 2H-$MoSe_2$, is diminished with increasing synthesis time, whereas a peak at 281 cm^{-1}, matching to E^1_{2g} of 1T-$MoSe_2$, was increased with the synthesis time, indicating the 1T phase of $MoSe_2$ increased as synthesis time increased.[14] Additionally, the peaks, which are related to 1T phase, is clearly observed for the synthesis time of 36 h (J_1=105 cm^{-1}, J_2=149 cm^{-1}, J_3=224 cm^{-1}) revealing the presence of mixed 1T and 2H phase of $MoSe_2$. [15] In the case of $MoSe_2$-P-6h, the peaks at 121, 198, 277, and 352 cm^{-1} is matched to MoO_x revealing the incomplete formation of $MoSe_2$.[16] **Figure S5 (a) and (b)** , shows the TEM images of the $MoSe_2$-P-36h and its selected area electron diffraction (SAED) pattern, exhibiting that synthesized $MoSe_2$ was polycrystalline in nature, reflected by the ring patterns in SAED with respective lattice spacing values of 0.67 and 0.28 nm, which correspond to (0 0 2) and (1 0 0) planes of 1T+2H phases of MoS_2. Furthermore, TEM-EDS elemental mapping analysis reveals the even distribution of elements Mo and Se in samples with higher intensity of Se being observed, as shown in **Figure S5** (c)-(e). We determined that the optimized synthesis time was 36 h based on the detailed material analysis revealing the presence of the 1T/2H mixed phases of $MoSe_2$ and revealed the complete transformation of precursors into $MoSe_2$ structures without the trace of unreacted Se. The composition of $MoSe_2$-P-36 h was $MoSe_{2.24}$ which was confirmed using inductively coupled plasma-mass spectrometry (ICP-MS). (**Table S1**) Moreover, 36 h sample exhibited highest HER performances under the 0.5 M H_2SO_4electrolyte, compared to samples synthesized at different time, where lowest overpotential of 177mV at 10mA/cm^2 and lowest charge transfer resistance was observed (R_{ct}= 22Ω). Furthermore, highest electrical double layer capacitance (59.06 mF/cm^2) was observed for the 36 h samples compared to the other samples with different synthesis time (**Figure S6** and**S7**).

After the optimization of the $MoSe_2$ powder synthesis, we conducted experiments to directly grow the 1T/2H mixed phase $MoSe_2$ on a conductive support such as carbon paper. Morphology and the microstructure of $MoSe_2$-I-36h was investigated using SEM and HR-TEM. As shown in **Figure 1** (b), dense and flower-like $MoSe_2$ nanosheets were grown on the carbon paper. In addition, through the HR-TEM analysis, the resultant

4

in-situ grown samples exhibited heterointerface of 1T/2H phases of MoSe$_2$ as shown in **Figure 1** (c) and (d). Elemental composition mapping was conducted using TEM-EDS elemental mapping technique where Mo and Se was well distributed along the samples with higher intensity being observed for the Se, like the 36h powder case. (**Figure S8**). After the Pt nanoparticle decoration, Pt clusters were observed on the MoSe$_2$ surface (**Figure 1** (e) and **Figure S9**). Furthermore, decorated Pt nanoparticle exhibited lattice spacing value of 0.20 nm, which corresponds to (200) plane, which was confirmed via HR-TEM analysis (**Figure S10**) . [17]
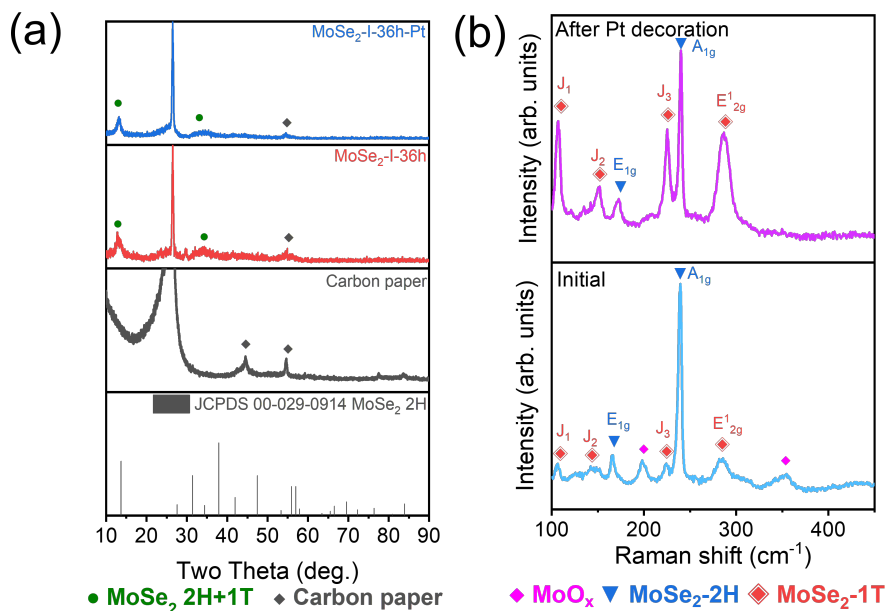
Figure 2. Comparison of MoSe2-I-36h after Pt decoration. a) X-ray diffraction (XRD) spectra; green sphere and grey diamond indicate MoSe$_2$ 1T/2H and carbon paper, b) Raman spectra of MoSe$_2$-I-36h; Magenta diamond, blue reverse triangle, and red diamond denote MoO$_x$, MoSe$_2$-2H, and MoSe$_2$-1T.

Figure 2 (a) displays XRD spectra of MoSe$_2$-I-36h before and after Pt cluster decoration. Similar to MoSe$_2$-P 36h case, MoSe$_2$-I-36h was composed of mixed phases of 1T/2H MoSe$_2$. After Pt decoration on the MoSe$_2$, the peaks matching to 1T/2H phases of MoSe$_2$ remained unchanged while Pt XRD peaks were not detected due to low concentration. From the Raman spectra in**Figure 2** (b), the intensity of the A$_{1g}$ peak (2H phase) was decreased, whereas those of J$_1$, J$_2$, J$_3$, and E$^1_{2g}$ (1T phase peaks) increased significantly after the Pt decoration, indicating the conversion of 2H MoSe$_2$ to 1T MoSe$_2$ during the Pt electrodeposition process. **Figure S11(a)** , shows the XPS analysis of the MoSe$_2$-I-36h-Pt sample where the presence of Pt element was clearly confirmed compared to the pristine MoSe$_2$-I-36h. Furthermore, the intensities of the peaks (229.3, 232.9 eV for Mo 3d and 54.7 and 55.7 eV for Se 3d, which were related to 2H-MoSe$_2$, were decreased while increase in relative intensities of the 1T-MoSe$_2$ were observed after the Pt electrodeposition process, as depicted in **Figures S11** (b) and (c) which is in good agreement with the Raman analysis.**Figures S11** (d) exhibit Pt 4f spectra, the peaks located at 72.5 and 75.6 eV corresponding to Pt^0 were observed, while the peaks located at 73.6 and 76.8 eV corresponding to Pt^{2+} might be attributed to the oxidation of Pt nanoparticles during the electrochemical reaction process.[18]

not-yet-known not-yet-known

not-yet-known

unknown

2.2 Electrochemical properties

5
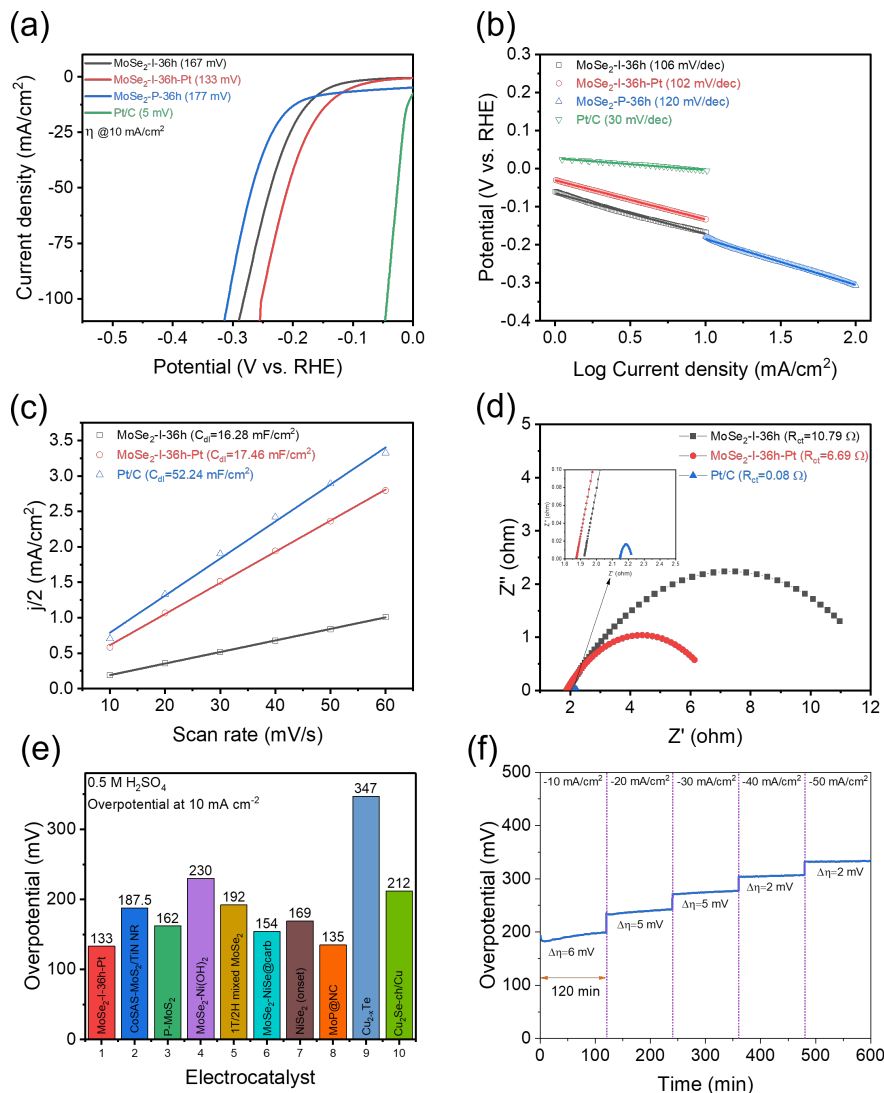
Figure 3. a) LSV curves with 85% iR correction at a scan rate of 5 mV/s, b) Tafel slope, c) C_{dl}, d) EIS, e) Comparison of HER overpotential at 10 mA cm^{-1} for previously reported HER electrocatalysts in 0.5 M H_2SO_4, f) Chronopotentiometry curves at 10, 20, 30, 40, and 50 mA/cm^{-1} in 0.5 M H_2SO_4.

HER performance of the $MoSe_2$ samples were evaluated under the acidic media (0.5 M H_2SO_4). LSV curves in **Figure 3** (a) shows that HER can be enhanced by direct growth approach on the current collector compared to conventional electrode preparation method. The loading amount onto the carbon paper of $MoSe_2$-P and $MoSe_2$-I samples was approximately 5 mg. $MoSe_2$-I-36h exhibited a lower η_{10} (167 mV) than that of $MoSe_2$-P-36h (177 mV). Furthermore, HER activity of $MoSe_2$-I-36h was significantly enhanced by in-situ electrodeposition of Pt cluster, resulting in η_{10} of 133 mV. The η_{10} without iR correction of $MoSe_2$-P-36h, $MoSe_2$-I-36h, $MoSe_2$-I-36h-Pt, and Pt/C were 196, 185, 150, and 23 mV, respectively (**Figure S12**). The lower Tafel slope, represents the higher intrinsic activity of the electrocatalyst. The Tafel slope values of $MoSe_2$-P-36h, $MoSe_2$-I-36h, $MoSe_2$-I-36h-Pt, and Pt/C were 120, 106, 102, and 30 mV/dec, respectively (Figure 3(b)). This suggests that $MoSe_2$-I-36h-Pt displayed higher intrinsic activity compared to the other $MoSe_2$ samples which can be confirmed by specific activity comparison (**Figure S13**). The double layer capacitance (C_{dl}) can be extracted from CV curves with different scan rate in non-Faradaic region (**Figure**

S14). The C_{dl} of MoSe$_2$-I-36h-Pt (17.46 mF/cm^2) was improved compared to MoSe$_2$-I-36h (16.28 mF/cm^2), as depicted in Figure 3(c). However, the C_{dl} of MoSe$_2$-P-36h (59.06 mF/cm^2) was larger than those of MoSe$_2$-I samples. The MoSe$_2$-P-36h was bonded using polyvinylidene fluoride (PVDF), however, the surface of carbon paper was exposed (**Figure S15** (a)), which may improve $C_{dl,}$ whereas MoSe$_2$-I-36h can be attributed to the even deposition of electrocatalyst on a carbon paper surface which minimized exposure of bare carbon paper which would contribute to additional capacitance (**Figure S15** (b) [19] as revealed in our previous study, the C_{dl} of pure carbon paper was highest compared to electrocatalyst-coated electrodes.[19] In addition, thicknesses of the MoSe$_2$-P-36h and MoSe$_2$-I-36h were over 1000 nm, 605 nm, respectively (**Figure S16**). Its large thickness could contribute to the increase in charge transfer resistance (R_{ct}) for MoSe$_2$-P-36h due to an increased charge transfer distance and presence of unwetted region leading to decreased active sties in the electrocatalysts.[20] Decoration of highly active and conductive Pt nanoparticles on MoSe$_2$ surface assisted in reducing the charge transfer resistance for MoSe$_2$-I-36h-Pt samples which lead to lowest R_{ct} values amongst the MoSe$_2$ based samples. As displayed in Figure S6(b) and Figure 3(d), R_{ct} values of MoSe$_2$-P-36h, MoSe$_2$-I-36h, MoSe$_2$-I-36h-Pt, and Pt/C were 22, 10.79, 6.69, and 0.08 Ω, respectively, suggesting that the lower interfacial resistance between the electrolyte and surface of electrocatalysts, while charge transfer is facilitated in MoSe$_2$-I-36h-Pt sample. Finally, MoSe$_2$-I-36h-Pt showed a lower HER overpotential with high specific mass activity in acidic media (0.5 M H$_2$SO$_4$) compared to other previously reported metal chalcogenide and MoSe$_2$ materials (Figure 3(e); **Table S3 & Table S4**). The stability of MoSe$_2$-I-36h-Pt was evaluated by chronopotentiometry (Figure 3(f)). MoSe$_2$-I-36h-Pt showed slight increase in overpotential by 6, 5, 5, 2, and 2 mV at a current density of 10, 20, 30, 40, and 50 mA/cm^2, respectively, where good HER stability was demonstrated under the varying current densities. Besides the HER stability evaluation at different current densities, we also performed long term stability test of the MoSe$_2$-I-36h-Pt under the acidic media (0.5 M H$_2$SO$_4$) at a current density of 10mA/cm^2. After the 100 h of stability test, MoSe$_2$-I-36h-Pt electrocatalyst exhibited slight increase in the overpotential (Δ17mV), revealing the good long-term stability of the resultant electrocatalyst under the acidic media. (**Figure S17**)

2.3 Characterizations of MoSe$_2$-I-36h-Pt after stability test
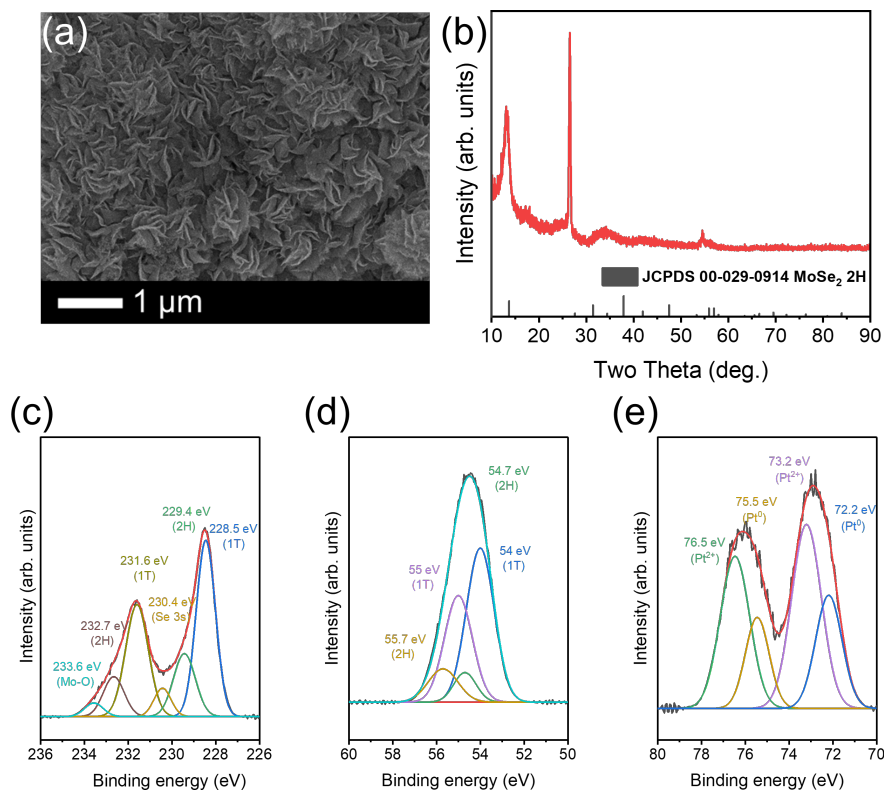
Figure 4. Characterization of $MoSe_2$-I-36h-Pt after stability test. (a) Post-test SEM image of surface, (b) Post-test XRD, (c) Post-test Mo 3d, (d) Post-test Se 3d, and (e) Post-test Pt 4f.

It is important to investigate the electrocatalyst's properties after the stability test. The post-test morphology of $MoSe_2$-I-36h was well maintained, as displayed in **Figure 4a** . XRD analysis reveals an increase in intensity of a peak at 13.1°, indicating the possible phase transformation from 1T to 2H-$MoSe_2$ during the stability test (Figure 4(b)). Moreover, such phase transition was confirmed by post-test Raman analysis where reduction in 1T phase $MoSe_2$ peaks were observed compared to the $MoSe_2$-I-36h-Pt sample before the test. (**Figure S18**) This could be attributed to differences in electrochemical stability between the 1T and 2H phase where, unstable 1T phase may undergo transformation to a more energetically favorable 2H phase of $MoSe_2$ during the stability test which may have resulted in slight increase in overpotential shown in Figure 3f. The post stability test, Mo 3d and Se 3d peak analysis also reveals the relative increase in the 2H peaks (Figure 4 (c) and (d)) compared to the sample before the stability test (Figure S11). These changes might have originated from the transformation of $MoSe_2$ from 1T to 2H-$MoSe_2$ phase during the stability test. However, the surface state of $MoSe_2$-I-36h-Pt still maintained 1T/2H mixed phases of $MoSe_2$ despite the phase conversion. With respect to Pt 4f, the binding energies were nearly unchanged (Figure 4(e)), suggesting the properties of Pt were rarely affected by the stability test.

2.4 DFT study of HER mechanism
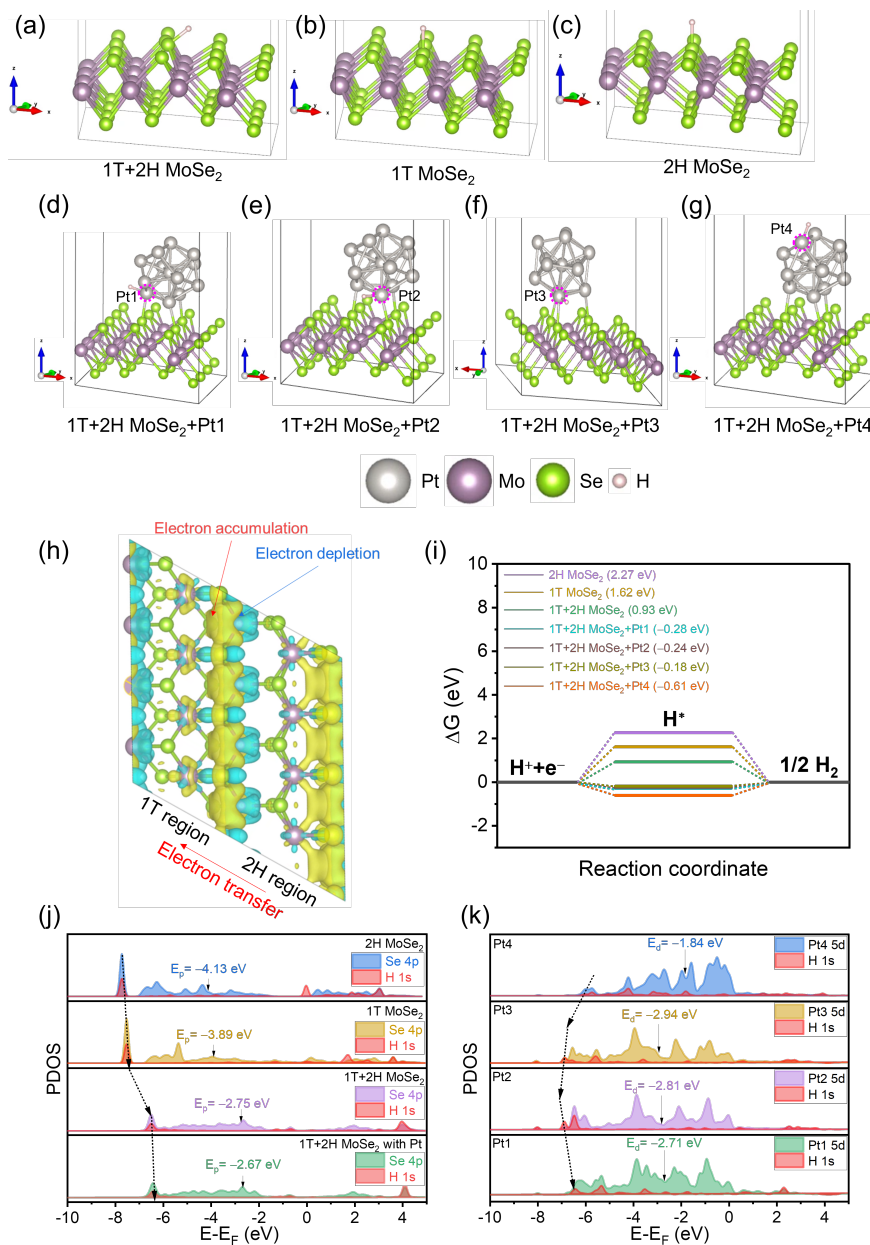
Figure 5. DFT calculations of MoSe₂ based electrocatalyst; Fully relaxed geometry. (a) 1T/2H MoSe₂, (b) 1T MoSe₂, (c) 2H MoSe₂. 1T/2H MoSe₂ with Pt cluster and the optimized geometry when H atom adsorbs different Pt positions; (d) Pt1, (e) Pt2, (f) Pt3, (g) Pt4. Grey, light purple, light green, and white ball indicate Pt, Mo, Se, and H, respectively, (h) Charge density difference of 1T/2H MoSe₂; yellow and blue contour are charge accumulation and depletion regions, respectively, (i) Gibbs free energy of HER with different active sites, (j) Partial density of states for Se 4p and H 1s; E_p indicates p-band center, (h) Partial density of states for Pt 5d; E_d indicates d-band center.

We conducted density functional theory (DFT) to reveal the role of heterostructure of 1T/2H mixed phases of MoSe₂ and the 1T/2H mixed phase MoSe₂ surface with Pt cluster. The fully relaxed MoSe₂ structures, which are 1T/2H MoSe₂, 1T MoSe₂, 2H MoSe₂, and 1T/2H MoSe₂ with Pt, respectively, were prepared for calculating the Gibbs free energy of hydrogen adsorption (ΔG_H), as illustrated in **Figure 5** (a)–(g).

9

As depicted Figure 5(h), the charge density accumulation was found for the interface between 1T and 2H $MoSe_2$, resulting in the enhanced HER activity.[21] The HER activity can be estimated by ΔG_H value. When the ΔG_H value approaches 0 eV, the HER activity increases owing to the optimal balance between the adsorption and desorption reaction of H atoms on the active sites.[22] The ΔG_H values of 1T/2H $MoSe_2$ of point 1, point 2, and point 3 are 1.76, 0.93, and 1.81 eV, respectively (**Figure S20** (a) and (b) in Supporting Information). Their corresponding structures are shown in Figure 5(a) and Figure S20(c) and (d) in the Supporting Information. Figure 5(i) shows ΔG_H values of 1T $MoSe_2$ (1.62 eV), 2H $MoSe_2$ (2.27 eV), 1T/2H $MoSe_2$ (0.93 eV), 1T/2H $MoSe_2$ with Pt1 (–0.28 eV), 1T/2H $MoSe_2$ with Pt2 (–0.24 eV), 1T/2H $MoSe_2$ with Pt3 (–0.18 eV), 1T/2H $MoSe_2$ with Pt4 (–0.61 eV). The 1T/2H $MoSe_2$ exhibits the lower ΔG_H values for the than those of individual 2H $MoSe_2$ and 1T $MoSe_2$ phases, indicating that the presence of heterointerfaces between 1T/2H phases in $MoSe_2$ enhances the HER activity. The improved HER activity may be attributed to the electron accumulation at the heterointerface, where optimized ΔG_H was observed at the interface between 1T MoS_2 and 2H MoS_2.[21] Furthermore, the presence of the Pt cluster improves HER activity of Se site at the heterointerface, showing lower Gibbs free energy of 0.88 eV (**Figure S21(a)**).

To investigate relationship between electronic structures and HER performance, we calculate partial density of states (PDOS) of 1T/2H $MoSe_2$ with Pt, 1T/2H $MoSe_2$, 1T $MoSe_2$, and 2H $MoSe_2$ for Se atom and H atom, as shown in **Figure 5** (j). The bonding strength of H atom at active site can be confirmed by p-band center (E_p). When E_p is upshifted to Fermi energy (E_F), the bonding strength is increased.[23] The E_p of 1T/2H $MoSe_2$ with Pt, 1T/2H $MoSe_2$, 1T $MoSe_2$, and 2H $MoSe_2$ for Se 4p were –2.67, –2.75, –3.89, and –4.13 eV, respectively. Upshift of PDOS of H 1s to E_F indicates the increased H atom activation, as observed in 1T/2H $MoSe_2$. Therefore, the electron accumulation at the heterointerface, improved the bonding strength between Se and H atom, leading to more favorable H activation which contributes to the increased HER activity. In addition, the Pt cluster promotes the HER activity at the heterointerface, which attributed to the modulation of electronic structure, as shown in Figure 5(j).

When d-band center (E_d) is close to E_F, the bonding strength of the adsorbate is enhanced. When H atom is adsorbed on different Pt sites, ΔG_H of Pt1, Pt2, Pt3, and Pt4 are –0.28, –0.24, –0.18, and –0.61 eV, respectively. E_d values of above sites are –2.71, –2.81, –2.94, and –1.84 eV, as depicted in **Figure 5** (i) and (k), indicating that the Pt1, Pt2, and Pt3 sites near the Se atoms are favorable for hydrogen adsorption and desorption. Although the Pt4 site shows the low HER activity, its site has higher HER activity than 1T $MoSe_2$, 2H $MoSe_2$, and 1T+2H $MoSe_2$. Additionally, as shown in **Figure S22** , Pt3 sites of 1T $MoSe_2$+Pt and 2H $MoSe_2$+Pt exhibit reduced Gibbs free energies (–0.24 and –0.23 eV), indicating the interaction between Pt and Se moderately control bonding strength of Pt and H regardless of the $MoSe_2$ slab types. 1T+2H $MoSe_2$ shows the lowest ΔG_H, indicating that heterostructure is more favorable for HER compared to 1T $MoSe_2$ and 2H $MoSe_2$ when the Pt cluster is decorated onto the substrate. Based on DFT results, the high HER activity of the 1T/2H $MoSe_2$+Pt cluster is attributed to the synergistic effect of the heterostructure of 1T/2H $MoSe_2$ and the Pt cluster.

In summary, we synthesize 1T/2H mixed phase $MoSe_2$ heterostructure directly grown on a carbon paper using a hydrothermal method. Pt cluster is decorated on the heterostructure using an in-situ electrochemical deposition approach. This two-step approach enhances the interfacial adhesion and reduces the interfacial resistance between the carbon paper and the electrocatalyst compared to that of using $MoSe_2$ powder with binder. As a result, directly grown sample ($MoSe_2$-I-36h) exhibits higher HER activity than the 1T/2H $MoSe_2$ powder ($MoSe_2$-P-36h) due to direct bonding between the substrate and electrocatalyst which improves charge transfer. In addition, the HER activity is significantly improved when the small amount of 0.15 wt% Pt was decorated on the heterostructure of 1T/2H $MoSe_2$. From DFT results, we found that the heterostructure interface (phase boundary between 1T and 2H $MoSe_2$) act as a site with low ΔG_H which would act as a primary active region in the electrocatalyst. Such reduction in ΔG_H at the phase boundary is attributed to the electron accumulation, improved H activation, and enhanced bonding strength between Se and H atom. In addition, the decorated Pt cluster act as not only an independent active site but also tuning the electronic structure both Pt and Se active site which enhanced the HER activity.

3. Conclusions

In this work, we successfully prepared self-standing 1T/2H mixed phases of $MoSe_2$ on a carbon paper using a direct growth approach via hydrothermal synthesis method, where post in-situ Pt decoration was carried out by electrodeposition method. The electrocatalyst (Pt decorated1T/2H mixed phase of $MoSe_2$) prepared by this simple two step approach exhibit high HER activity (133 mV at 10 mA/cm^2) under the acidic medium (0.5 M H_2SO_4). The direct growth of 1T/2H mixed phase $MoSe_2$ on a carbon paper contributes to the lower R_{ct} with reduction in the overpotential by 10 mV at a current density of 10 mA/cm^2 compared to the electrocatalyst prepared by conventional (electrocatalyst + binder) approach. Moreover, low concentration (0.15 wt%) decoration of Pt contributes to significant enhancement in the HER activity with further reduction in R_{ct} compared to the pristine 1T/2H $MoSe_2$ electrocatalyst without the Pt deposition. Such results are well supported by the DFT calculation and provides insight on enhanced HER activity at the phase boundary region in $MoSe_2$ compared to the 1T or 2H alone regions due to the electron accumulation at the heterointerface, while Pt clusters interacts with Se site in $MoSe_2$ while perturbing the electronic states of $MoSe_2$, which further improves the HER activity and confirmed through ΔG_H and E_d analysis, highlighting a origin of phase dependent HER performances in $MoSe_2$ based electrocatalyst in the presence of a dopant, which will pave a way for developing advanced metal dichalcogenide 2D material based electrocatalyst in future.

4. Experimental sections

Sodium molybdate dihydrate ($Na_2MoO_4[?]2H_2O$, 99.5% purity; Sigma aldrich), selenium powder (Se, 99.5% purity, Sigma aldrich), sodium borohydride ($NaBH_4$, 97% purtiy; Daejung), and ethanol (C_2H_5OH, 99.5% purity; Daejung) were used without purification. Deionized (DI) water of 18.2 MΩ cm^{-1} was obtained using a water purification system (V-RO up 15-S, A.F ENG, Korea).

4.2 Preparation of MoSe$_2$ powder with 2H.

To obtain pristine 2H $MoSe_2$, the synthesis procedure was the same in section 2.1, and the synthesized solution was slow cooled to 25 °C in a furnace.

4.3 Preparation of 1T/2H mixed phase MoSe$_2$ directly grown on a carbon paper.

To synthesize $MoSe_2$ directly onto a carbon paper (HCP020N; Shanghai Hesen Electric Co. Ltd), a mixed solution containing precursors and a 2×4 cm^2 carbon paper was transferred to a 100 mL stainless-steel autoclave. The synthesis duration was 36 h, and the solution was rapidly cooled to 25 °C within 15 min. In-situ $MoSe_2$ with varying synthesis times denoted $MoSe_2$-I-Y (Y = 36), where I represent 'in-situ' and Y represent synthesis time. The loading amount onto the carbon paper was about ˜5 mg. For the Pt loading on the $MoSe_2$-I-36h-Pt sample was 0.15 wt% (˜7.5ug/cm^2).

4.4 Preparation of Pt/C electrode

Pt/C (nominally 20% on carbon black, Thermo Fisher Scientific) 30 mg and 5 mg polyvinylidene fluoride (PVDF) were mixed in 500 µL N-methyl-2-pyrrolidone (NMP). The 50 µL ink solution was deposited evenly onto a 1×1 cm^2 carbon paper. The electrode was dried in an oven at 80 °C for 24 h. The loading amount onto the carbon paper was about ˜5 mg.

4.5 Material properties

The morphologies of the $MoSe_2$ samples were observed through scanning electron microscopy (SEM, Philips, XL30 ESEM-FEG) at the MEMS Sensor Platform Center of SungKyunKwan University (SKKU). The microstructures of the samples were monitored by field-emission TEM (FE-TEM, JEOL LTD, JEM-2100F) at an accelerating voltage of 200 kV. To exactly observe Pt cluster on the $MoSe_2$-I-36h-Pt, a focused ion beam (FIB, FEI, Quanta 3D FEG) was selected. Elemental analysis of Mo, Se, and Pt was conducted using inductively coupled plasma mass spectrometry (ICP-MS, PerkinElmer, NexION2000). Phase identification of as-synthesized $MoSe_2$ samples was performed using multiple-purpose X-ray diffraction (XRD, Rigaku, SmartLab 9kW) with Cu K$_\alpha$ source (λ = 0.15406 nm, 45 kV, 200 mA) in the range of 10–90°. In the case

11

of MoSe$_2$-I samples, grazing-incidence XRD method at an 0.5° was chosen to avoid the strong intensity of a substrate. The surface states were characterized using a Raman spectrometer (HORIBA, LabRam HR Evolution) with 532 nm laser in the range of 100–400 cm^{-1} and X-ray photoelectron spectroscopy (XPS, Vg Scienta, EASC 2000) with an Al anode.

4.7 Density functional theory (DFT)

Quantum ESPRESSO (QE) code version 7.2 was used to theoretically determine the effect of the heterostructure and Pt decoration.[27] The projected augmented wave (PAW) pseudopotentials were employed to show core–valence interactions. The Perdew–Burke–Ernzerhof (PBE) functional of the generalized gradient approximation (GGA) was used. The Van der Waals force was also corrected using the "Grimme-D3" code, built in QE. The cutoff values, including the plane-wave wavefunction of 55 Ry and charge density of 310 Ry, were considered for convergence. A smearing code (marzari-vanderbilt) was introduced to enhance the convergence.

The crystallographic information file (CIF) of MoSe$_2$(mp-1634) on Materials Project website was used to design the supercell.[28] The supercell of MoSe$_2$ was optimized using the Broyden–Fletcher–Goldfarb–Shanno (BFGS) algorithm with a force threshold of 3.8×10^{-4} Ry/Bohr ([?]0.01 eV/) and a total energy convergence threshold of $1.0x10^{-5}$ Ry ([?]0.0001 eV). The Monkhorst-pack k-point grid of 4 x 4 x 1 was selected to obtain the optimized structure without spin polarization calculation owing to non-magnetic property.[29] Additionally, to prevent interactions between the periodic boundaries along the z-axis, a vacuum of 20 was applied in the supercell. Subsequently, the Gibbs free energies (ΔG) of the reactions in the HER mechanism for MoSe$_2$ and MoSe$_2$ with Pt cluster were calculated and are presented below.[23]

$$\Delta G_H = \Delta E_H + \Delta E_{\text{ZPE}} - T\Delta S_H \quad (4)$$

$$\Delta E_H = E_{\text{MoSe}_2+H} - E_{\text{MoSe}_2} - \frac{1}{2}E_{H_2} \quad (5)$$

where ΔG_H is the Gibbs free energy of hydrogen adsorption. ΔE_H, $E_{\text{MoSe2+H}}$, E_{MoSe2}, and E_{H2} is the adsorption energy of hydrogen, the total energies of the MoSe$_2$ slab with hydrogen and the same structure without hydrogen, respectively. E_{H2} indicates the total energy of a gas-phase hydrogen molecule. ΔE_{ZPE} and ΔS_H represent the changes in zero-point energy, entropy between the adsorbed atomic hydrogen and hydrogen in gas phase, respectively.

The DOS of 2H MoSe$_2$, 1T+2H MoSe$_2$, and 1T+2H MoSe$_2$ with Pt cluster were calculated for a k-point grid of $6 \times 6 \times 1$ to obtain the exact electronic structure. To reveal heterostructure effect, p-band center of Se (E_p) was calculated using following equation:[23]

$$E_p = \frac{\int_{-\infty}^{+\infty} E \times \rho dE}{\int_{-\infty}^{+\infty} \rho \delta E}, (6)$$

where E_p, ρ, and E represent the p-band center, density of p states projected onto the Se atom, and energy level, respectively. When Pt cluster was decorated on the heterostructure slab, d-band center (E_d) was estimated as follows:[24]

$$E_d = \frac{\int_{-\infty}^{+\infty} E \times \rho dE}{\int_{-\infty}^{+\infty} \rho \delta E}, (7)$$

Author contribution

J.H.P and S. W. K contributed equally to this work. J.H.P and S. W. K conducted experiments data curation & analysis and manuscript preparation. J.C.R, S. J. P, and S.Y.L contributed to data analysis. Conceptualization, Supervision and writing—review and editing was conducted by D.H.S, H.J.K and S.J.S.

Acknowledgements

Conflicts of Interest

The authors declare no conflict of interest.

References

[1] J. Zhu, L. Hu, P. Zhao, L. Y. S. Lee, K.-Y. Wong, *Chemical Reviews* 2020, *120* , 851.

[2] S. Chandrasekaran, M. Khandelwal, F. Dayong, L. Sui, J. S. Chung, R. Misra, P. Yin, E. J. Kim, W. Kim, A. Vanchiappan,*Advanced Energy Materials* **2022** , 12, 2200409.

[3] Y. Luo, Z. Zhang, M. Chhowalla, B. Liu, *Advanced Materials* **2022** , 34, 2108133.

[4] D. Jeon, D. Y. Kim, H. Kim, N. Kim, C. Lee, D. H. Seo, J. Ryu,*Advanced Materials* **2024** , 36, 2304468.

[5] J. Wang, F. Xu, H. Jin, Y. Chen, Y. Wang, *Advanced materials* **2017** , 29, 1605838.

[6] a) H. Shi, H. Zhang, M. Li, Y. Wang, D. Wang, *Journal of Alloys and Compounds* **2021** , 878, 160381; b) W. Xiao, D. Bukhvalov, Z. Zou, L. Zhang, Z. Lin, X. Yang, *ChemSusChem* **2019** , 12, 5015; c) J. Wu, B. Li, Y. Shao, X. Wu, Y. Sun,*Journal of materials science* **2020** , 55, 2129.

[7] M. Jiang, J. Zhang, M. Wu, W. Jian, H. Xue, T.-W. Ng, C.-S. Lee, J. Xu, *Journal of Materials Chemistry A* **2016** , 4, 14949.

[8] Y. Qu, H. Medina, S. W. Wang, Y. C. Wang, C. W. Chen, T. Y. Su, A. Manikandan, K. Wang, Y. C. Shih, J. W. Chang, *Advanced Materials* **2016** , 28, 9831.

[9] H. Li, L. Zhu, C. Li, Z. Wu, H. Li, Q. Chen, Y. Huang, X. Zhu, Y. Sun, International Journal of Hydrogen Energy 2022, 47, 30371.

[10] X. Ren, F. Wu, Y. Wang, Q. Ou, F. Li, *New Journal of Chemistry* **2024** , 48, 5160.

[11] R. Chen, C. Yang, W. Cai, H.-Y. Wang, J. Miao, L. Zhang, S. Chen, B. Liu, *ACS energy letters* **2017** , 2, 1070.

[12] a) J. Hao, K. Wu, C. Lyu, Y. Yang, H. Wu, J. Liu, N. Liu, W.-M. Lau, J. Zheng, *Materials Horizons* **2023** ; b) Y. Zhang, S. Zhang, Y. He, H. Li, T. He, H. Shi, X. Ma, Q. Yang, L. Chen, J. Chen,*Journal of Solid State Chemistry* **2021** , 298, 122108.

[13] X. Li, L. Zhao, J. Yu, X. Liu, X. Zhang, H. Liu, W. Zhou,*Nano-Micro Letters* **2020** , 12, 1.

[14] Y. Yin, Y. Zhang, T. Gao, T. Yao, X. Zhang, J. Han, X. Wang, Z. Zhang, P. Xu, P. Zhang, *Advanced Materials* **2017** , 29, 1700311.

[15] U. Gupta, B. Naidu, U. Maitra, A. Singh, S. N. Shirodkar, U. V. Waghmare, C. Rao, *Apl Materials* **2014** , 2.

[16] Y. Liu, S. Liu, H. Li, L. Yu, L. Sun, J. Xue, R. Xu, G. Chen,*Materials Chemistry and Physics* **2022** , 278, 125657.

[17] R. Chen, Z. Cao, Z. Lyu, M. Xie, Y. Shi, Y. Xia,*ChemNanoMat* **2019** , 5, 599.

[18] X. Tian, X. Cui, Y. Xiao, T. Chen, X. Xiao, Y. Wang, *ACS Applied Materials & Interfaces* **2023** , 15, 9604.

[19] J.-H. Park, J. C. Ro, S.-J. Suh, *Current Applied Physics* **2022** , 42, 50.

[20] L. Yu, S. Sun, H. Li, Z. J. Xu, *Fundamental Research* **2021** , 1, 448.

[21] Z. Hong, W. Hong, B. Wang, Q. Cai, X. He, W. Liu,*Chemical Engineering Journal* **2023** , 460, 141858.

[22] J. Deng, H. Li, J. Xiao, Y. Tu, D. Deng, H. Yang, H. Tian, J. Li, P. Ren, X. Bao, *Energy & environmental science* **2015** , 8, 1594.

[23] C. Meng, Y. Gao, Y. Zhou, K. Sun, Y. Wang, Y. Han, Q. Zhao, X. Chen, H. Hu, M. Wu, *Nano Research* **2023** , 16, 6228.

[24] G. Zhan, Y. Yao, F. Quan, H. Gu, X. Liu, L. Zhang,*Journal of Energy Chemistry* **2022** , 72, 203.

[25] J.-H. Park, J. C. Ro, S.-J. Suh, *Applied Surface Science* **2022** , 589, 153041.

[26] J. H. Nam, M. J. Jang, H. Y. Jang, W. Park, X. Wang, S. M. Choi, B. Cho, *Journal of Energy Chemistry* **2020** , 47, 107.

[27] P. Giannozzi, O. Andreussi, T. Brumme, O. Bunau, M. B. Nardelli, M. Calandra, R. Car, C. Cavazzoni, D. Ceresoli, M. Cococcioni,*Journal of physics: Condensed matter* **2017** , 29, 465901.

[28] A. Jain, S. P. Ong, G. Hautier, W. Chen, W. D. Richards, S. Dacek, S. Cholia, D. Gunter, D. Skinner, G. Ceder, *APL materials* **2013** , 1.

[29] C. M. Bastos, R. Besse, J. L. Da Silva, G. M. Sipahi,*Physical Review Materials* **2019** , 3, 044002.